ELSEVIER

Polymer 42 (2001) 3223–3231

polymer

www.elsevier.nl/locate/polymer

# Elongational flow-induced morphology change of block copolymers. 2. A polystyrene-*block*-poly(ethylene butylene)-*block*-polystyrene triblock copolymer with cylindrical microdomains

T. Kotaka[a,*], M. Okamoto[a], A. Kojima[a,1], Y.K. Kwon[a], S. Nojima[b]

[a]*Advanced Polymeric Materials Engineering, Graduate School of Engineering, Toyota Technological Institute, Hisakata 2-12-1, Tempaku, Nagoya 468-8511, Japan*

[b]*Japan Advanced Institute of Science and Technology (JAIST) — Hokuriku, School of Materials Science, Tatsunokuchi, Ishikawa 923-12, Japan*

Received 16 June 2000; received in revised form 31 July 2000; accepted 2 August 2000

**Abstract**

Elongational flow behavior of a polystyrene-*block*-poly(ethylene butylene)-*block*-polystyrene (SEBS) triblock copolymer melt with cylindrical morphology is investigated by elongational flow opto-rheometry (EFOR), transmission electron microscopy (TEM) and small angle X-ray scattering (SAXS). The SEBS film is first roll-processed to align the PS cylinders in a preferred direction. The uniaxial elongation is applied either parallel (denote Case I) or perpendicular (Case II) to the cylinder axis. Transient tensile stress $\sigma(\dot{\epsilon}_0; t)$ and birefringence $\Delta n(\dot{\epsilon}_0; t)$ are measured with a constant Hencky strain rate $\dot{\epsilon}_0$ ranging from 0.01 to 1.0 $s^{-1}$ at various temperatures between PS glass transition, $T_{g(PS)}$, and the order–disorder transition, $T_{ODT}$, of the SEBS. The data suggest that either the PS or PEB domains is preferentially elongated in the early stage of elongation, depending on the initial alignment of the cylinder phase. On further elongation, the elongational viscosity of the Case I melt exhibits strain-induced softening behavior in the final stage of elongation, whereas that of the Case II melts clearly displays strain-induced hardening behavior. The TEM and SAXS data of the samples elongated with a $\dot{\epsilon}_0 = 1.0\ s^{-1}$ show that the cylinders are mostly inclined approximately by 40–50° to the direction of elongation, whereas they are mostly aligned, parallel to the elongation direction on slower elongation. The morphology of highly elongated SEBS melts is governed by the applied strain rate and temperature, regardless of the initial orientation of the cylinders. 

*Keywords*: Elongational viscosity; Birefringence; Polystyrene-*block*-poly(ethylene butylene)-*block*-polystyrene

## 1. Introduction

In the preceding paper [1], we reported rheo-optical behavior under uniaxial elongation of a polystyrene-*block*-poly (ethylene butylene)-*block*-polystyrene-*block*-poly(ethylene butylene) (SEBSEB) tetrablock copolymer melt with spherical morphology using elongational flow opto-rheometry (EFOR) [2,3], small angle X-ray scattering (SAXS) and transmission electron microscopy (TEM). The EFOR employed was a Meissner's elongational rheometer [4] combined with a high-precision birefringence optics, which enabled us to measure simultaneously transient tensile stress $\sigma(\dot{\epsilon}_0; t)$ and birefringence $\Delta n(\dot{\epsilon}_0; t)$ of polymer melts as a function of time $t$ and Hencky strain rate $\dot{\epsilon}_0$.

The rheological and morphological behavior of the SEBSEB melt varied with the elongation conditions [1]. Under low $\dot{\epsilon}_0$ (0.01 $s^{-1}$) at high temperatures (160 and 170°C), the PS spheres were considerably elongated and aligned to the elongation direction, exhibiting strain-induced hardening behavior. On the other hand, under high $\dot{\epsilon}_0$ (1.0 $s^{-1}$) at low temperatures (130 and 150°C), they were slightly deformed and inclined by approximately 45° to the elongation direction, showing strain-induced softening or rupturing behavior. The birefringence $\Delta n(\dot{\epsilon}_0; t)$ was increased significantly with time, $t$, with a $\dot{\epsilon}_0 = 0.01\ s^{-1}$ at high temperatures, but slightly increased under a $\dot{\epsilon}_0 = 1.0\ s^{-1}$ at low temperatures. Thus the stress optical coefficient [5–7] $C(\dot{\epsilon}_0; t)[\equiv \Delta n(\dot{\epsilon}_0; t)/\sigma(\dot{\epsilon}_0; t)]$ of the SEBSEB melt varied with $t$, rather than with $\sigma(\dot{\epsilon}_0; t)$ or Hencky strain $\epsilon(\equiv \dot{\epsilon}_0 t)$. The $C(\dot{\epsilon}_0; t)$ measured with a $\dot{\epsilon}_0 = 1\ s^{-1}$ at low

* Corresponding author. Tel.: +81-52-809-1860; fax: +81-52-809-1864.
*E-mail address:* kotaka@toyota-ti.ac.jp (T. Kotaka).

[1] Present address: Toray Industry Ltd, Ooe-cho 9-1, Minato-ku, Nagoya 455-8502, Japan.

0032-3861/01/$ - see front matter 
PII: S0032-3861(00)00596-6

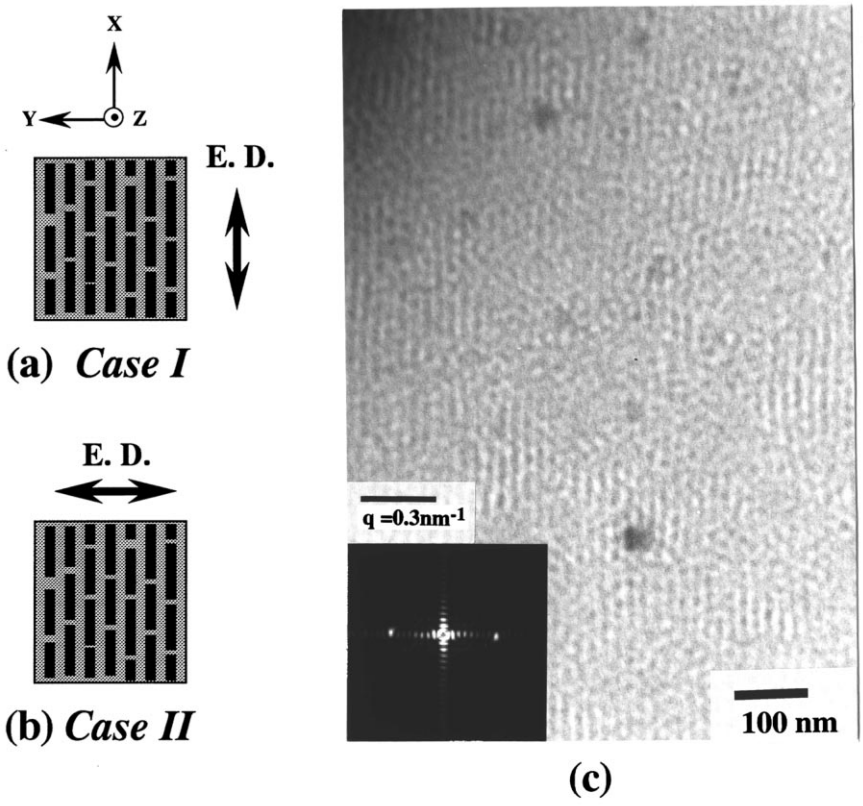


Fig. 1. The schematic representation of the (a) Case I ( ‖ ) and (b) Case II ( ⊥ ) melt and (c) TEM micrograph in the $x$–$y$ plane of the roll-processed SEBS film. The insert in the left corner shows the corresponding fast Fourier transform (FFT) image. The E.D. denotes the elongation direction of the film, as shown in arrow.

temperatures remained almost constant and close to that of PEB chain, whereas the $C(\dot{\epsilon}_0; t)$ measured with low $\dot{\epsilon}_0$ at high temperatures increased enormously. These data pointed out that the stress optical rule (SOR) did not hold for the SEBSEB melt, probably due to the contribution of the form birefringence $\Delta n_f$ of the deformed PS domains. The SAXS and TEM measurements revealed that the original spherical PS domains of the SEBSEB melt were almost maintained on fast elongation, whereas they were mostly elongated to form cylinders on slow elongation, leading to a large contribution of $\Delta n_f$.

These results motivated us to investigate the elongational flow behavior of block copolymer melts with anisotropic cylindrical morphology. The material investigated was a symmetric polystyrene-*block*-poly(ethylene butylene)-*block*-polystyrene (SEBS) triblock copolymer that showed the PS cylinder morphology in the continuous PEB matrix. The alignment of the cylinders was achieved by roll-processing the compression-molded SEBS films in a preferred direction. These roll-cast films were set to be elongated along the direction either parallel or perpendicular to the cylinder axis. The TEM and SAXS data of the unelongated and elongated samples were also collected and compared with the elongation viscosity and birefringence data determined from the EFOR measurements.

## 2. Experimental

### 2.1. Materials

A symmetric SEBS triblock copolymer with PS weight fraction of 20.9% (the corresponding volume fraction $\phi_{PS} = 0.19$; Asahi Chemical Co.) was used in this study. Its melt flow index (MFR) was 0.38 g min$^{-1}$ at 230°C under 2.16 kgw load; and the order–disorder transition temperature, $T_{ODT}$, was approximately 230°C, as determined from temperature dependence of isochronal dynamic moduli (see Section 3.1.3). The molecular weights were determined by gel permeation chromatography (GPC) using PS elution standards. The weight-average molecular weight, $M_w$, was 72.6 kg mol$^{-1}$, the number-average, $M_n$, 66.0 kg mol$^{-1}$and the polydispersity index, $M_w/M_n$, around 1.15. The block sequence of the SEBS block copolymer was then estimated to be 6.9, 52.2 and 6.9 for PS, PEB and PS in the unit of kg mol$^{-1}$. The GPC chromatogram showed that the sample contained a small amount (less than 3 wt%) of a high molecular weight ($M_n \sim 132$ kg mol$^{-1}$) component. However, it was used without removing this high $M_n$ component.

### 2.2. Sample preparation

Specimens subjected to EFOR and other measurements

were prepared by the following procedures. The flat films with random orientation of the PS cylinders were initially obtained by either compression molding below the $T_{ODT}$ or solution casting. Then, they were roll-processed at 160°C for about 10 min by applying high shear strain along a chosen direction in order to induce the alignment of the PS cylinders in one direction. The roll-processed films were then placed between polyimide films (Kapton® HN, Toray-Du Pont) and again compression-molded at 5 MPa with a laboratory hot press at 260°C ($>T_{ODT} \sim 230$°C) for 6 min. Then, they were transferred to another hot-press kept at ambient temperature and pressure without applying load, and cooled by circulating chilled water into the jacket of the hot-press. The obtained sheet was about 1.8 mm thickness and was kept at room temperature prior to the measurements.

For dynamic moduli measurements, disks of a diameter $d \sim 25$ mm were punched out from the film. For EFOR measurements, sample strips of about 60 (length) × 7.0 (width) × 1.8 (thickness) $mm^3$ were prepared by cutting the sheet in the direction either parallel or perpendicular to the cylinder axis. The thickness direction of the sample strip was taken as $z$-axis direction and the directions parallel (length direction) and perpendicular (width direction) to the cylinder axis were assigned as $x$-axis and $y$-axis direction, respectively. The sample strips were elongated either in the $x$-axis (Case I), or in the $y$-axis direction (Case II) (see Fig. 1). The elongated samples were collected at various stages of elongation and rapidly quenched in ice water. The final sample strips were kept at room temperature and then subjected to the SAXS and TEM measurements.

### 2.3. Characterization methods

#### 2.3.1. Refractive indices

The refractive indices $n_x$ $n_y$ and $n_z$ of the roll-processed films were measured along the $x$-, $y$- and $z$-axis direction, respectively, at room temperature on a three-dimensional birefringence analyzer (KOBRA-21DH, Oji Scientific Instruments).

#### 2.3.2. TEM

TEM measurement of the unelongated and elongated SEBS samples was carried out at Tokyo Institute of Technology. Ultra-thin sections were obtained by microtoming each sample with a diamond knife on a Reichert Ultracut N/SC4E at −100°C, well below the glass transition temperature of the PEB block, $T_{g(PEB)}$, ($\sim -70$°C). The PS domains were stained with $RuO_4$ vapor at 50°C for 2 h. A TEM (EM H-300, Hitachi Co) was operated at an acceleration voltage of 100 kV. A Fast Fourier transform (FFT) analysis was carried out on the digitally saved TEM images with a commercial software (Ultimage®; Graftek France). These FFT images often contain a crisscross line due to the size and/or the frame of the TEM image for calculation.

#### 2.3.3. SAXS

For SAXS measurement, we used CuKα radiation (wavelength $\lambda = 0.154$ nm) generated from an X-ray generator (MAC Science M18X) operated at 40 kV and 30 mA. The angular dependence of SAXS intensity was monitored with a point-focusing optics and a one-dimensional position sensitive proportional counter (PSPC) of the effective length of 100 mm, held at a distance of 400 mm from the sample. The data were usually collected for 50 min.

#### 2.3.4. Dynamic mechanical analysis

Dynamic mechanical analysis of the unelongated specimens was conducted on a Rheometrics Dynamic Analyzer (RDA II, Rheometrics Scientific) with a parallel-plate geometry of ~25.0 mm diameter disks. Temperature dependence of dynamic $G'$, loss $G''$ moduli and their ratio, $G''/G'$ ($= \tan\delta$) was measured in the range of $30 \le T(°C) \le 260$. Temperature dependence of the complex moduli was also monitored in an oscillatory shear mode under an isochronal condition at a fixed frequency of $\omega = 0.1$ rad $s^{-1}$ and a strain amplitude of $\gamma = 2.0\%$ to avoid complication due to nonlinear responses of the sample.

#### 2.3.5. EFOR

Simultaneous measurement of transient tensile stress $\sigma(\dot{\epsilon}_0; t)$ and birefringence $\Delta n(\dot{\epsilon}_0; t)$ was conducted as a function of Hencky strain rate $\dot{\epsilon}_0$ and elongation time $t$ in our recently developed EFOR [2,3], which was a Meissner's new elongational rheometer (commercialized as RME from Rheometric Scientific Co.) combined with a birefringence monitor. The details on the principles and procedures of the EFOR measurements were described in our preceding papers [1,2].

For roll-processed SEBS films with PS cylindrical morphology, we conducted EFOR runs in both $x$- and $y$-axis direction. The measurement was made at three different temperatures, 150, 160 and 170°C, between $T_{g(PS)}$ (~100°C) and $T_{ODT}$ (~230°C) of the SEBS sample, and with three different Hencky strain rates, $\dot{\epsilon}_0$, of 0.01, 0.1 and 1.0 $s^{-1}$ at each temperature and investigated the effect of the strain rate on the morphological change of the aligned cylinder phase of the elongated SEBS films.

## 3. Results

### 3.1. Characterization of roll-processed SEBS films with aligned PS cylinders

#### 3.1.1. Refractive indices

The refractive indices, $n_x$, $n_y$ and $n_z$, of the roll-processed SEBS film were measured at room temperature in the $x$-, $y$-, and $z$-axis direction, respectively, as schematically shown in Fig. 1. The results were $n_x \approx n_y > n_z$ : 1.5342, 1.5341 and 1.5337 for $n_x$, $n_y$ and $n_z$, respectively. The difference $\Delta n_{fxy} (= n_x - n_y)$ measured on the $xy$ plane

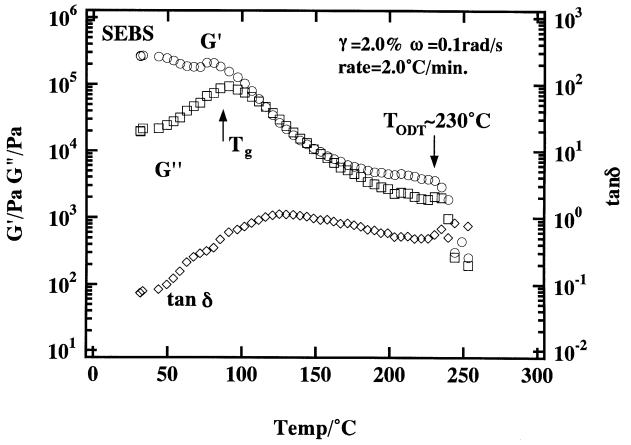


Fig. 2. Temperature dependence of the dynamic $G'$, loss G$''$ moduli and loss tan $\delta(= G''/G')$ for the unelongated SEBS specimen under isochronal condition at $\omega = 0.1$ rad s$^{-1}$ and the strain amplitude $\gamma = 2.0\%$ at a heating rate of 2°C/min.

was almost negligible (of the order of $10^{-4}$), whereas those $\Delta n_{fxy}(= n_y - n_z)$ and $\Delta n_{fxy}(= n_z - n_x)$ were either positive or negative with a similar magnitude of the order of $4 \times 10^{-4}$. The $\Delta n_{fyz}$ and $\Delta n_{fzx}$ were larger than the $\Delta n_{fxy}$ due to the structural anisotropy of the PS cylinder phase in the roll-processed SEBS film, in addition to the difference between the refractive indices of PS (1.59) and PEB domain (1.50).

### 3.1.2. TEM results

Fig. 1(c) showed a typical TEM micrograph of a roll-processed SEBS film, microtomed parallel to the $x$-axis direction. In this figure, the dark area represented the PS domains, stained with $RuO_4$. It showed a layered texture, mostly aligned along the $x$-axis direction. The average thickness of this layer was approximately 29 nm, which roughly corresponded to the diameter of the PS cylinders. The insert in the figure was an FFT image of the TEM micrograph, showing an intense peak at $q \sim 0.22$ nm$^{-1}$ on the equator. The TEM data with the FFT image indicated that the PS cylinders in the initial roll-cast sample were mostly aligned parallel to the $x$-axis direction, with the diameter, $D$, of approximately ~29 nm.

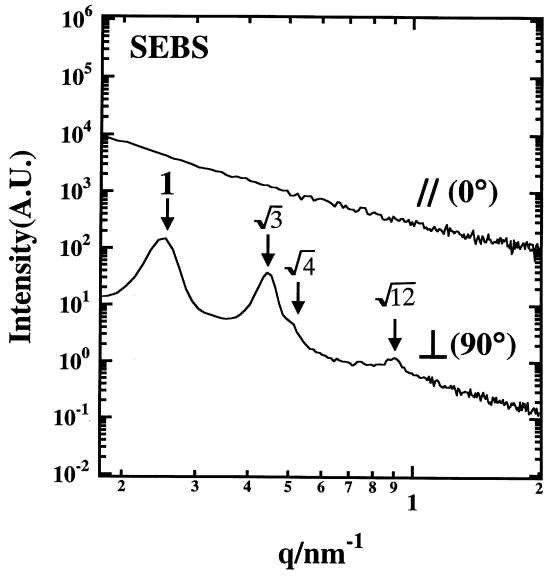


Fig. 3. Typical SAXS scan data of the roll-processed SEBS film: the top and bottom scans show the data measured in the $x$-axis and $y$-axis directions.

### 3.1.3. Dynamic mechanical analysis

Dynamic temperature sweep experiments were carried out under isochronal condition with the angular frequency of $\omega = 0.1$ rad s$^{-1}$, in order to determine the $T_{ODT}$ of the unelongated SEBS sample. The heating rate used was 2°C/min. Fig. 2 showed temperature dependence of the $G'$, $G''$ and tan $\delta$ of the unelongated SEBS film, in the range of $30 \leq T(°C) \leq 260$, in which the $G'$ and $G''$ decreased rapidly near 230°C, marked as a downward arrow, revealing the existence of the ODT. The data shown in this study were similar to those reported by Rosedale et al. [8]. Additional slope change in the $G'$ and $G''$ data was also observed near 95°C, marked as an upward arrow, due to the existence of the $T_g$ of the isolated PS cylinder domains.

### 3.1.4. SAXS results

Fig. 3 showed double logarithmic plots of relative SAXS intensities $I(q)$ vs. scattering vector, $q$ [$= (4\pi/\lambda) \sin \theta$ where $2\theta$ was the scattering angle] of the roll-processed, initial SEBS film, measured in the $x$- (top) and $y$-axis (bottom) direction. The orientation of the PS cylinders was set to be along the $x$-axis direction of the film. The raw data were corrected for background scattering and direct transmittance of the primary X-ray beam. The data measured in the $x$-axis direction have been multiplied by a factor of $10^3$ to avoid overlapping between two scan data.

In the top figure, the scattered intensity monotonously decreased with $q$ and no peak was found in this scan. In the bottom figure, we observed an intense peak at $q \sim 0.25$ nm$^{-1}$ and additional higher order peaks at $q$s (nm$^{-1}$) of ~0.43, 0.50 and 0.89, which were in the ratio of $1{:}\sqrt{3}{:}2{:}\sqrt{12}$. These results suggested that the nicely aligned PS cylinders along the $x$-axis direction were packed in a two-dimensional hexagonal lattice. The interdomain spacing $D[= (2/\sqrt{3})d_{100}$, where $d_{100}$ was the $d$-spacing of the maximum peak intensity] was estimated as approximately 28.5 nm, based on the position of the main peak intensity and close to the value (~29 nm) measured in the TEM experiments. The difference between the top and bottom data revealed that the cylindrical phase of the roll-processed SEBS film was highly anisotropic.

## 3.2. Characterization of the elongated SEBS films

### 3.2.1. Tensile stress and apparent retardation

In the EFOR measurements, the roll-processed SEBS film

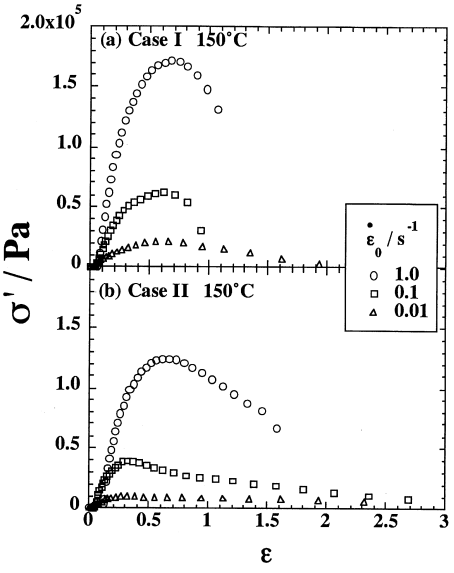


Fig. 4. The plots of engineering stress $\sigma'(\dot{\epsilon}_0; t) = F(\dot{\epsilon}_0; t)/A_0$ vs. Hencky strain $\epsilon(\equiv \dot{\epsilon}_0 t)$ curves of the (a) Case I and (b) Case II melt at 150°C with the strain rates $\dot{\epsilon}_0 = 1.0$ (○), 0.1 (□) and 0.01 (△) $s^{-1}$.

was stretched in the direction either parallel (Case I) or perpendicular (Case II) to the PS cylinder axis. Fig. 4(a) and (b) showed plots of engineering stress, $\sigma'(\epsilon)[\equiv F(t)/A_0]$ vs. Hencky strain $\epsilon(\equiv \dot{\epsilon}_0 t)$ of the Case I and II melt, respectively, measured at 150°C. Three values of the

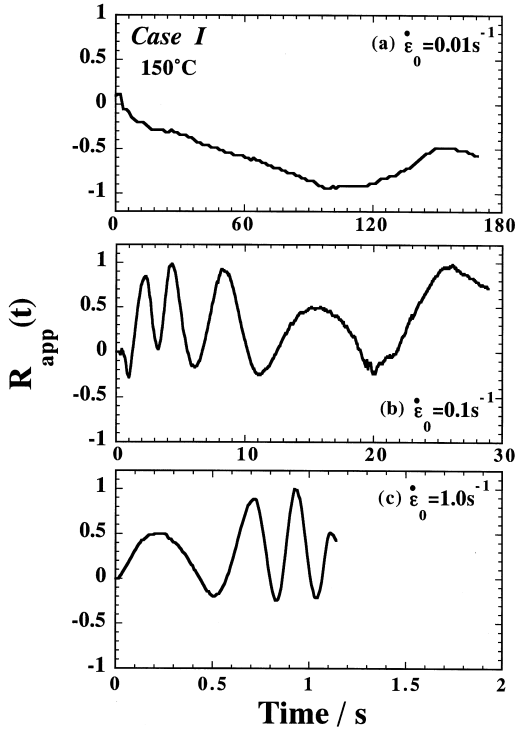


Fig. 5. Time dependence of the apparent retardation $R_{app}(t)$ of the Case I sample, measured during EFOR experiment with a strain rate $\dot{\epsilon}_0$ of: (a) 0.01; (b) 0.1; and (c) 1.0 $s^{-1}$.

Hencky strain rate $\dot{\epsilon}_0$ (0.01, 0.1 and 1 $s^{-1}$) were used for these measurements.

Although the attainable maximum Hencky strain $\epsilon_{max}(\equiv \dot{\epsilon}_0 t_{max})$ was approximately 7, most of samples were ruptured much earlier than the $\epsilon_{max}$. Fig. 4(a) and (b) showed that the Case I and II melts were ruptured at $\epsilon$s up to around 2 and 3, respectively. The total elongation times for the Case I melt were approximately 1, 10 and 200 s at elongation with $\dot{\epsilon}_0 =$ 1, 0.1, and 0.01 $s^{-1}$, whereas those for the Case II melts were approximately 1.5, 30 and 250 s for $\dot{\epsilon}_0 = 1$, 0.1 and 0.01 $s^{-1}$, respectively.

The initial modulus defined as the initial slope of each figure increased with $\dot{\epsilon}_0$. At each $\dot{\epsilon}_0$, the slope and maximum stress, $\sigma'_{max}$, of the Case I melt were about twice larger than those of the Case II melt, whereas the ultimate elongation at break, $\epsilon_{max}$, of the Case II melt was larger than that of the Case I melt. The measured $\epsilon_{max}$s of both melts did not show any systematic change with strain rate $\dot{\epsilon}_0$, probably due to the defects preexisted in the roll-cast samples. Higher initial modulus for the Case I melt indicated that the PS cylinders were initially elongated in the Case I melt elongation, whereas the PEB matrix was preferentially elongated in the early stage of the Case II melt elongation.

Figs. 5 and 6 showed the apparent retardation $R_{app}(t)$ vs. elongation time $t$ of the Case I and II melt, respectively, measured during the elongation with $\dot{\epsilon}_0 = 0.01$, 0.1 and 1.0 $s^{-1}$. In these figures, the complicated time dependence of the $R_{app}(t)$ was due to not only the different elongation behavior of the PS and PEB domain in the Case I and II melt, especially in the early stage of elongation, but also the contribution of the form birefringence $\Delta n_f$ of the isolated PS cylindrical domains. Note that typical values of $\Delta n$ for the PS and PEB melts are negative and positive, respectively [5,9,10]. In Fig. 5, the negative $R_{app}(t)$s in the beginning of the Case I melt elongation with $\dot{\epsilon}_0 = 0.01$ and 0.1 $s^{-1}$ were probably due to the preferential elongation of the PS cylinders, whereas the initial positive $R_{app}(t)$ for the rapid elongation with $\dot{\epsilon}_0 = 1.0\ s^{-1}$ was due to the preferential deformation of the PEB matrix in the beginning. In Fig. 6, the fact that the initial positive values of the $R_{app}(t)$ for all $\dot{\epsilon}_0$ implied that the soft PEB matrix was preferentially elongated in the beginning of the Case II elongation, regardless of the applied strain rate.

### 3.2.2. Elongational viscosity

Figs. 7 and 8 showed the elongational viscosity, $\eta_E(\dot{\epsilon}_0; t)[\equiv \sigma(\dot{\epsilon}_0; t)/\dot{\epsilon}_0]$ and absolute values of birefringence $|\Delta n(\dot{\epsilon}_0; t)|$ of the Case I and II sample, respectively, plotted against the elongation time $t$. The data were collected at 150, 160 and 170°C. The shear viscosity, $\eta_0(\dot{\gamma}; t)$, of the unelongated sample was also measured at 150°C with a shear rate of $\dot{\gamma} = 0.001\ s^{-1}$ and included in Figs. 7(a) and 8(a), as shown in the solid curves. Both Case I and II samples showed neither a linear region, where $\eta_E(\dot{\epsilon}_0; t)$ $[\cong 3\eta_0(\dot{\gamma}; t)]$ was independent of $\dot{\epsilon}_0$, nor the steady state, where $\eta_E(\dot{\epsilon}_0; t)$ was constant and independent

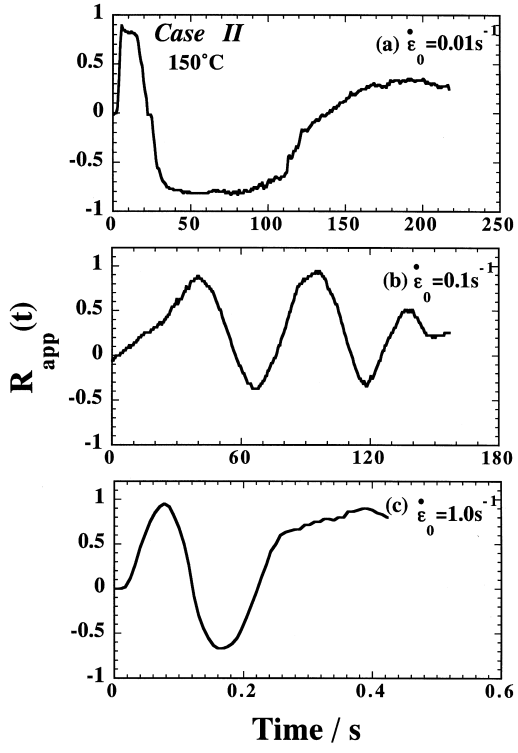


Fig. 6. Time dependence of the apparent retardation $R_{app}(t)$ of the Case II sample, measured during EFOR experiment at a strain rate $\dot{\epsilon}_0$ of: (a) 0.01; (b) 0.1; and (c) 1.0 $s^{-1}$.

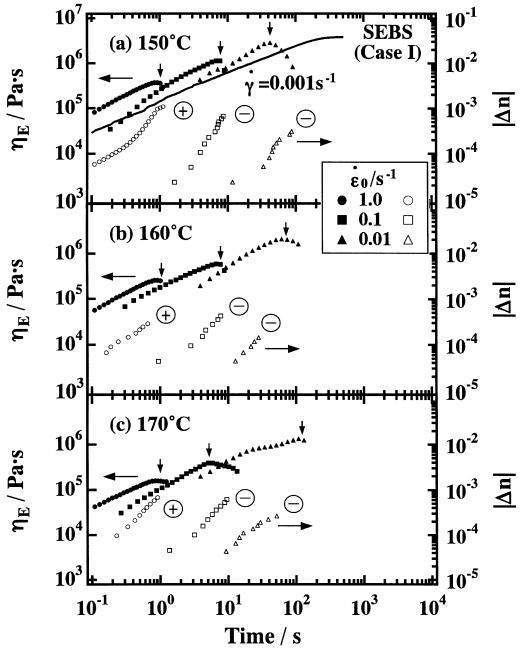


Fig. 7. Time dependence of the elongational viscosity $\eta_E(\dot{\epsilon}_0;t)$ [$\equiv \sigma(\dot{\epsilon}_0;t)/\dot{\epsilon}_0$] and the absolute values of birefringence $|\Delta n(\dot{\epsilon}_0;t)|$ of the Case I sample elongated at (a) 150; (b) 160; (c) 170°C with three different $\dot{\epsilon}_0$ indicated. The open symbols represent the elongational viscosity data and the closed symbols, the birefringence data. The solid line in (a) represents three times of the shear viscosity, $3\eta_0(\dot{\gamma};t)$, taken with a low shear rate of $\dot{\gamma} = 0.001\ s^{-1}$ on a cone-plate rheometer (RDAII). The signs in the circles on the birefringence data indicate actual signs of the measured values.

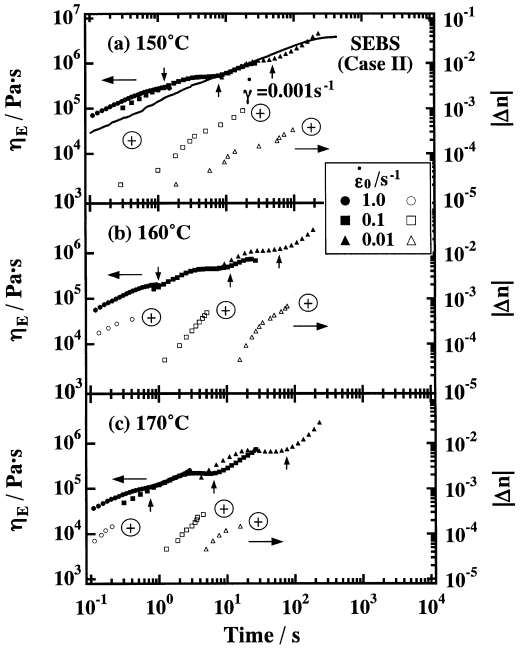


Fig. 8. Time dependence of $\eta_E(\dot{\epsilon}_0;t)$ [$\equiv \sigma(\dot{\epsilon}_0;t)/\dot{\epsilon}_0$] and $|\Delta n(\dot{\epsilon}_0;t)|$ of the Case II sample elongated at (a) 150; (b) 160; (c) 170°C with three different $\dot{\epsilon}_0$ indicated. The open symbols represent the $\eta_E(\dot{\epsilon}_0;t)$ data and the closed symbols, the $|\Delta n(\dot{\epsilon}_0;t)|$ data. The solid line in (a) shows again $3\eta_0(\dot{\gamma};t)$, taken with $\dot{\gamma} = 0.001\ s^{-1}$ on a cone-plate rheometer (RDAII). The signs in the circles on the birefringence data indicate actual signs of the measured values.

of $t$. The extended Trouton rule, $3\eta_0(\dot{\gamma};t) \cong \eta_E(\dot{\epsilon}_0;t)$ [11] did not hold for both cases.

In Fig. 7, the $\eta_E(\dot{\epsilon}_0;t)$ of the Case I melts started to decrease at $t_{\eta E}^{down}$, marked with the downward arrow, where the strain-induced softening or strain-induced rupturing took place. For the Case II melts shown in Fig. 8, the $\eta_E(\dot{\epsilon}_0;t)$s measured with $\dot{\epsilon}_0 = 0.01$ and $0.1\ s^{-1}$ began to increase at $t_{\eta E}^{up}$, marked with the upward arrow, where the strain-induced hardening behavior became prominent. However, those measured with $\dot{\epsilon}_0 = 1.0\ s^{-1}$ at low temperatures ($\leq$160°C) only showed strain-induced softening behavior. Note that the strain-induced hardening behavior of ordinary homopolymer melts takes place at a certain Hencky strain, $\epsilon_{\eta_E}$ ($= \dot{\epsilon}_0 \cdot t_{\eta_E} \sim$ constant) which is insensitive to either strain rate $\dot{\epsilon}_0$ or elongation temperature. For example, the value of $\epsilon_{\eta_E}$ of low-density polyethylene (LDPE) melt was about 1.6 in the ranges of $130 \leq T(°C) \leq 150$ and $0.005 \leq \dot{\epsilon}_0(s^{-1}) \leq 1.0$ [3]. The imposed stress is transferred to the domains and grains to be realigned and reorganized along the stretching direction. They are highly aligned along the stretching direction through the recombination and annihilation of structures, displaying the strain-induced hardening behavior, especially for the Case II elongation with slow strain rates.

The complicated time development of the $\eta_E(\dot{\epsilon}_0;t)$ and $\Delta n(\dot{\epsilon}_0;t)$ shown in Figs. 7 and 8 suggested that the stress optical rule (SOR) [5–7] did not hold for the SEBS melts.

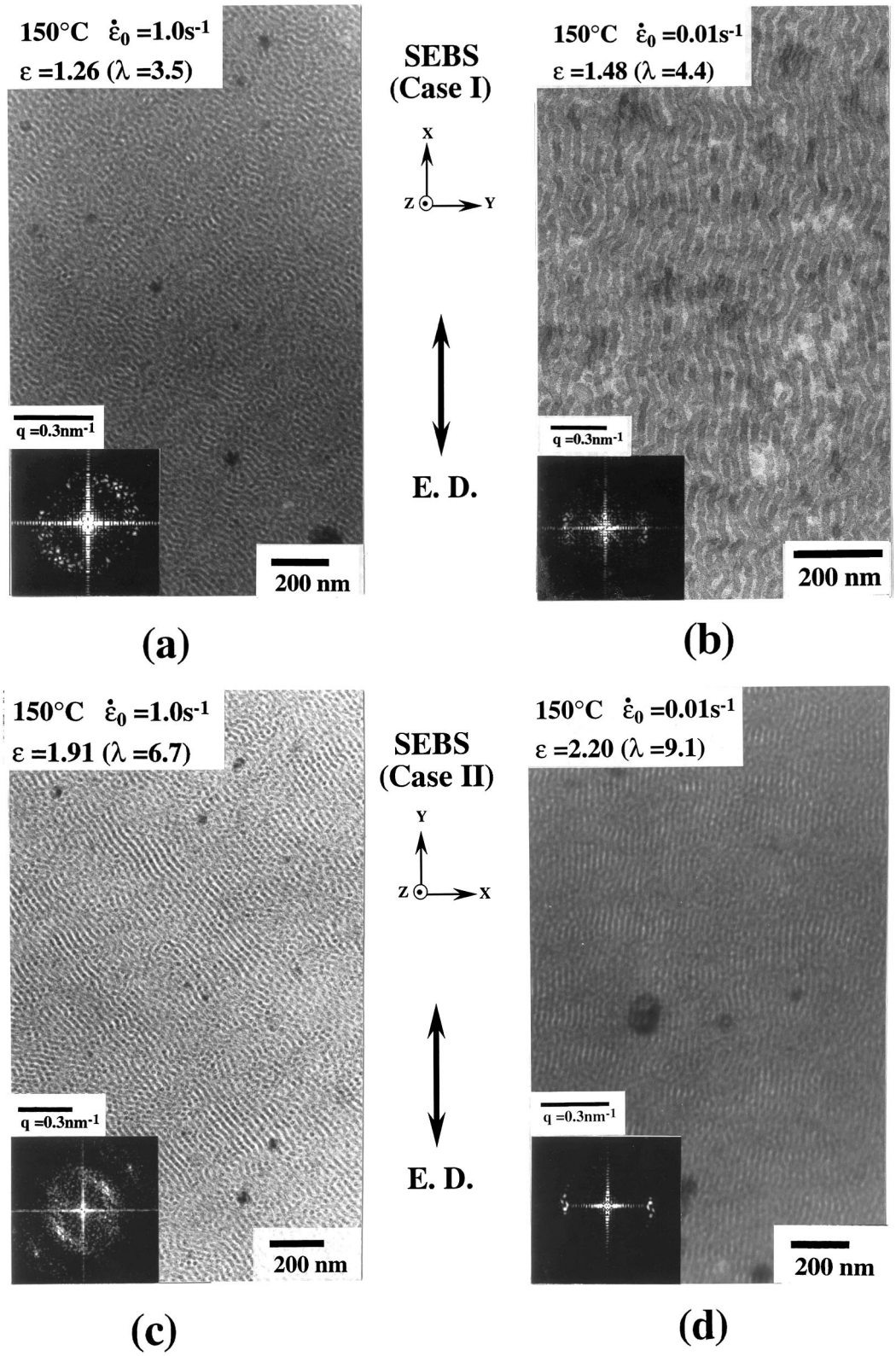


Fig. 9. TEM micrographs of the SEBS sample elongated at 150°C by (a) $\epsilon = 1.26$ ($\lambda = 3.5$) with $\dot{\epsilon}_0 = 1.0\ s^{-1}$ and (b) $\epsilon = 1.48$ ($\lambda = 4.4$) with $\dot{\epsilon}_0 = 0.01\ s^{-1}$ in the Case I elongation; (c) $\epsilon = 1.91$ ($\lambda = 6.7$) with $\dot{\epsilon}_0 = 1.0\ s^{-1}$ and (d) $\epsilon = 2.20$ ($\lambda = 9.1$) with $\dot{\epsilon}_0 = 0.01\ s^{-1}$ in the Case II elongation. The inserts in the micrographs are the corresponding FFT images.

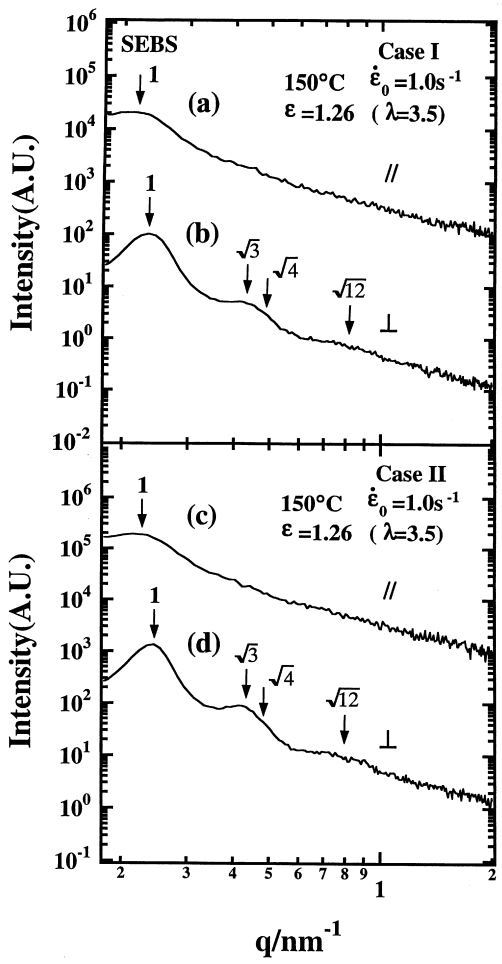


Fig. 10. SAXS data of the Case I (top) and II (bottom) samples elongated with $\dot{\epsilon}_0 = 1.0\ s^{-1}$ ($\epsilon = 1.26$ and $\lambda = 3.5$) at 150°C recorded in the directions parallel [(a) and (c)] and perpendicular [(b) and (d)] to the cylinder axis.

These results also reflected different elongational behavior of the PS and PEB domains especially in the early stage, as well as the form birefringence from the elongated PS cylindrical domains. In the initial stage of the Case I melt elongation, the $\Delta n(\dot{\epsilon}_0; t)$ was positive with a $\dot{\epsilon}_0 = 1.0\ s^{-1}$, whereas it was negative with $\dot{\epsilon}_0 = 0.01$ and $0.1\ s^{-1}$. However, in the initial stage of the Case II melt elongation, the $\Delta n(\dot{\epsilon}_0; t)$ was always positive with all three different strain rates. The negative birefringence in the early stage of the Case I melt elongation with lower $\dot{\epsilon}_0 (\leq 0.01\ s^{-1})$ indicated the preferential elongation of the PS domains, whereas the deformation of the PEB chains was prominent in the early stage of the Case II melt, resulting in the positive birefringence. The detailed analysis on the time evolution of the $\Delta n(\dot{\epsilon}_0; t)$ will be reported in a separate paper [12].

### 3.3. TEM and SAXS results of elongated SEBS film

#### 3.3.1. TEM results

Fig. 9 showed TEM micrographs of the Case I sample, elongated at 150°C up to Hencky strain of (a) $\epsilon = 1.26$ (stretching ratio $\lambda = 3.5$) with $\dot{\epsilon}_0 = 1.0\ s^{-1}$; (b) $\epsilon = 1.48$ ($\lambda = 4.4$) with $\dot{\epsilon}_0 = 0.01\ s^{-1}$, and the Case II sample, elongated up to (c) $\epsilon = 1.19$ ($\lambda = 6.7$) with $\dot{\epsilon}_0 = 1.0\ s^{-1}$; (d) $\epsilon = 2.20$ ($\lambda = 9.1$) with $\dot{\epsilon}_0 = 0.01\ s^{-1}$. Upon fast elongation with $\dot{\epsilon}_0 = 1.0\ s^{-1}$ shown in Fig 9(a) and (c), the PS cylinders of both melts were inclined to the stretching direction. Their FFT images shown in the left corner of the TEM micrographs displayed peak intensities centered at approximately $+45°$ and $-135°$ from the equator.

Fig. 9(b) and (d) showed that both melts displayed the cylindrical phase, mostly aligned along the stretching direction. The FFT image shown in the left corner of each figure showed equatorial peak intensity, confirming the parallel alignment of the elongated PS cylinders to the elongation direction. Based on the peak positions in the FFT images in Fig. 9, the average domain spacings of the elongated PS cylindrical phases of both melts were estimated to be around 28–30 nm. The similarities of the TEM micrographs between Fig. 9(a) and (c) and between Fig. 9(b) and (d) also pointed out that the elongated morphology of the cylinder phase at large deformation was not controlled by initial orientation of the domains, but the applied strain rate.

#### 3.3.2. SAXS results

Fig. 10 showed SAXS scan data of the roll-cast films, elongated at 150°C with $\dot{\epsilon}_0 = 1.0\ s^{-1}$ up to $\epsilon = 1.26$ ($\lambda = 3.5$), measured in the directions (a) parallel and (b) perpendicular to the elongation direction of the Case I melt, and (c) parallel and (d) perpendicular to the elongation direction of the Case II melt. The data shown in both panels were almost the same, indicating that the final morphologies of the elongated Case I and II melt were almost the same under these experimental conditions. These data also confirmed the TEM results, showing that the final morphology of the highly elongated samples was controlled by the strain rate, not by the initial morphology of the samples.

The existence of the peak at around $q \sim 0.21\ nm^{-1}$ in Fig. 10(a) and (c) and the broadness of the peaks in Fig. 10(b) and (d) were appeared due to the inclination of the cylinder phase and increased structural disorder at high degree of elongation. In Fig. 10(b) and (d), the intense 100 peak intensity was found at $q \sim 0.23\ nm^{-1}$ and the broadness of the peak at $q \sim 0.45\ nm^{-1}$ was due to the overlap between 110 and 200 peak. These peak intensities pointed out that the hexagonal packing of the cylinders was maintained during elongation with a fast strain rate, even with slight inclination to the stretching direction. The difference between the top and bottom figure in both panels also indicated that the structural anisotropy of the cylinder phase was persisted.

The SAXS data of the Case I and II melt, elongated with a slow strain rate showed almost the same features as shown in Fig. 3, indicating that the hexagonally packed cylinders were highly aligned along the stretching direction. Especially for the Case II melt, the parallel realignment of the

cylinders was generated by the rotation and reorganization of the grain and domain structure into the stretching direction. The realignment process of the cylinders of both melts were different, but their final morphologies were almost the same. Their structural changes and realignment process of the cylinders associated with slow elongation will be reported in a separate publication [12].

## 4. Discussion

The elongational flow-induced deformation behavior of the SEBS samples was dependent on the initial morphology of the cylindrical phase. Time development of the engineering stress and apparent retardation of the Case I and II melt was different due to not only the preferential elongation of either of both domains in the early stage of elongation, but also the deformation and the rotation of the cylinder domains and grains developed during elongation. The latter caused a significant deviation from the value predicted by the SOR, mainly due to a large contribution of the form birefringence of the isolated PS cylinders. The TEM and SAXS data also pointed out that the highly elongated morphologies of both melts were dependent on the applied strain rate, rather than on the initial morphology of the cylinder phase.

The TEM data shown in Fig. 9(a) and (c) showed the inclination of the cylinder phase, elongated with a fast strain rate, by approximately 40–50° to the elongation direction. Pakula et al., reported the inclination of the PS cylinders of a polystyrene-*block*-polybutadiene-*block*-polystyrene (SBS) triblock copolymer during elongation below $T_{g(PS)}$ and described that the molecular orientation of the polybutadiene chains in the matrix prevented the random orientation of the PS cylinders to be aligned into the stretching direction [13]. In our experiment, the inclination of the cylinder domains was generated by the rapid elongation process at high temperatures between the $T_{g(PS)}$ and $T_{ODT}$, which prevented a gradual realignment and reorganization process of the grain and domain structure and caused an early rupture at defects during elongation.

The elongation with slow strain rates ranging between 0.1 and 0.01 $s^{-1}$ at high temperatures generated highly aligned morphologies of both Case I and II melt, probably due to the rotation and reorganization of the grain and domain structure. The similar one-dimensional SAXS profiles of the unelongated and elongated samples pointed out that the grain structure was rotated by elongation. In addition, the TEM data shown in Fig. 9(b) and (d) also showed that the cylindrical domain structures of both melts were slightly distorted. These results pointed out that both the domain and grain structure were deformed and reoriented by high degree of elongation.

## 5. Conclusions

Simultaneous measurements of transient tensile stress $\sigma(\dot{\epsilon}_0; t)$ and birefringence $\Delta n(\dot{\epsilon}_0; t)$ provided information on the morphological changes of the block copolymer melts subjected in a uniaxial elongation. The strain-induced softening and hardening behavior of the cylinder microstructure depended on the initial alignment of the cylinder morphology, applied strain rate, and temperature. In the early stage of elongation, the PS and PEB domains in the Case I and II melt were deformed differently due to the initial orientation of the cylinder phase. The elongation with a fast strain rate led to the inclined morphology, due to the rapid rotation of the grain structure that led to the early rupture of the samples. The final morphology of the elongated samples was controlled by the applied strain rate and temperature due to the deformation and rotation of the domains and grains, rather than by the initial original orientation of the cylinders prior to elongation.

## Acknowledgements

The authors thank Dr Tuneo Chiba and Prof. Takashi Inoue at Tokyo Institute of Technology for TEM measurement.

## References

[1] Kotaka T, Okamoto M, Kojima A, Kwon YK, Nojima S. Polymer 2000;42:1207.
[2] Kotaka T, Kojima A, Okamoto M. Rheol Acta 1997;36:646.
[3] Okamoto M, Kojima A, Kotaka T. Polymer 1998;39:2149.
[4] Meissner J, Hostettler J. Rheol Acta 1994;33:1.
[5] Janeschitz-Kriegl H. Polymer melt rheology and flow birefringence. New York: Springer, 1983.
[6] Doi M, Edwards SF. The theory of polymer dynamics. Oxford: Clarendon Press, 1986.
[7] Treloar LRG. The physics of rubber elasticity. 3rd ed. Oxford: Clarendon Press, 1975.
[8] Rosedale JH, Bates FS. Macromolecules 1990;23:2329.
[9] Janeschitz-Kriegel H. Adv Polym Sci 1969;6:170.
[10] White JL. Principles of polymer engineering rheology. New York: Wiley, 1990.
[11] Schlund B, Utracki LA. Polym Engng Sci 1987;27:359.
[12] Kobori Y,Kwon YK, Okamoto M, Kotaka T. Macromolecules (submitted).
[13] Pakula T, Saijo K, Kawai H, Hashimoto T. Macromolecules 1985;18:1294.